Parameters of Electric Currents in Active Regions with Different Levels of Flare Productivity and Different Magnetomorphological Types

Yu. A. Fursyak[a,]*, V. I. Abramenko[a], and A. V. Zhukova[a]

[a] Crimean Astrophysical Observatory, Russian Academy of Sciences, Crimea, 298409 Russia
*e-mail: yuriy_fursyak@mail.ru

Abstract—In this paper, the magnetic-field and electric-current parameters are calculated for a sample of 73 active regions (ARs) of solar activity cycle 24 based on magnetographic data from the Helioseismic and Magnetic Imager (HMI) instrument aboard the Solar Dynamics Observatory (SDO). The calculated values are compared to the level of flare productivity and features of the AR morphology. The following results are obtained. (1) The imbalance of local vertical electric currents in the regions of the studied sample does not exceed a few percent (the maximum obtained value is 8.08%), in contrast to the magnetic-flux imbalance, which can reach a few tens of percent (the maximum absolute value is 82.11%). (2) The highest correlation of the calculated parameters of electric current with the level of AR flare productivity is observed for the total unsigned vertical electric current $\overline{I_{z\,\text{tot}}}$ (a Pearson correlation coefficient of $k = 0.67$) and the average unsigned vertical electric current density $\left\langle \overline{|j_z|} \right\rangle$ ($k = 0.66$), which are averaged over the AR monitoring period. (3) It is shown that the values of the electric-current parameters for the Ars in which the basic empirical laws of the Babcock−Leighton dynamo theory are violated are higher than the corresponding values of the electric current parameters for the regular ARs. This result may indicate that there is additional energy pumping by the local dynamo mechanisms in the irregular regions.

INTRODUCTION

Electric currents and magnetic fields are an important component of the totality of complex phenomena occurring in the solar atmosphere. Within the nonstationary processes occurring in the upper layers of the solar atmosphere, electric currents transform the energy of nonpotential magnetic fields (the so-called "free" magnetic energy (Wang et al., 1996; Schrijver et al., 2008)) into other forms, such as kinetic or thermal energy. Therefore, electric currents are directly involved in solar flares, because the flare process, to a first approximation, is a rapid dissipation of excess energy of magnetic fields.

It is believed that there are two possible mechanisms of electric-current emergence in an active region (AR). In the first, electric currents arise on the surface due to the shear or rotational motions of spots at the photospheric level (McClymont and Fisher, 1989; Török and Kliem, 2003; Aulanier et al., 2005; Dalmasse et al., 2015). The second mechanism can be called the depth mechanism, because, in this case, a magnetic tube is twisted in the convective zone of the Sun (in the sub-photospheric layers, or at its depth); a magnetic flux then comes to the surface with its own electric current system already formed (Leka et al., 1996; Longcope and Welsch, 2000; Cheung and Isobe, 2014). In any case, the electric current systems are formed in ARs as a response to the increasing complexity of the magnetic configuration due to motion.

There are many classifications describing the complexity of the AR magnetic fields. Two classifications are most widely used today. These are the Zurich evolutionary classification, which was subsequently modified by P.S. McIntosh (1990). It primarily describes the sunspot group size and some morphological features. The Mount Wilson classification (Hale et al., 1919) characterizes the complexity of the AR magnetic fields without regard to its evolutionary status. These two classifications have both advantages and disadvantages; in some cases, they are combined (e.g., see information on the websites https://solarmonitor.org or https://tesis.lebedev.ru).

Over the last few years, the Crimean Astrophysical Observatory (CrAO) of the Russian Academy of Sciences has been developing a magnetomorphological classification (MMC) of ARs (Zhukova, 2018; Abramenko et al., 2018) that essentially combines the advantages of the two aforementioned classifications.

It is known that there are three main laws for the morphology of an AR magnetic field: Hale's polarity law, Joy's law for the tilt angle of the spot group axis, and the rule of predominance of the leading polarity spot area. The latter is referred to one of the following three types depending on whether these laws are observed or not in a particular AR. The first type includes regions of group A ("correct" or regular), for which all of the above laws are observed. For the second AR group, B ("irregular"), at least one of the above laws is violated. Within this classification, multipolar regions also belong to type B. The third type consists of unipolar regions of the U type. They are considered remnants of the leading spots of the A or B type regions depending on whether or not the ARs observe Hale's law.

We studied the relationship between the electric-current parameters and the level of AR flare productivity in an earlier paper (Fursyak et al., 2020). Here, we continue the study of these relationships, but we use more extensive material. In addition, an important question in the context of AR research is whether there are differences between the values of the electric-current parameters in the regions of different magnetomorphological types. Following physical principles the ARs of type B according to the MMC should have higher values of the electric-current parameters, since violation of the main laws by sunspot groups implies the operation of mechanisms not only of the mean field dynamo but also of the local dynamo. The study of this issue is an important objective of our study.

2. OBSERVATIONAL DATA

The analysis is based on data from the Helioseismic and Magnetic Imager instrument onboard the Solar Dynamics Observatory (HMI/SDO, Scherrer et al., 2012), a set of SHARP (Spaceweather HMI/SDO Active Region Patches, Bobra et al., 2014; Hoekshema et al., 2014) magnetograms of magnetic-field vector components at photospheric level available on the Joint Science Operations Center (JSOC) website http://jsoc2.stanford.edu/ajax/lookdata.html (data series hmi.sharp_cea_720s). The electric-current parameters are calculated based on data on the structure of magnetic fields in the studied ARs.

In order to establish the nature of the relationship between the electric-current parameters in the photosphere and the type of area according to the MMC, we used the Magnetomorphological Classification catalog available on the Crimean Astrophysical Observatory (CrAO) website (https://sun.crao.ru/databases/catalog-mmc-ars).

Additional information on the phase of development of the studied ARs and their flare productivity during our observation period was obtained from the resources at https://tesis.lebedev.ru, http://solar.dev.argh.team/sunspots (developed by R.K. Zhigalkin, CrAO), https://satdat.ngdc.noaa.gov/sem/goes/data/

full/ (GOES-15 satellite data on the X-ray radiation flux in the wavelength range of 1−8 Å in the Earth's orbit), and-https://www.lmsal.com/solarsoft/ latest_events_archive.html.

We analyzed 73 ARs of solar cycle 24. The time interval for the monitoring of the analyzed ARs sample was limited to the time of their location within $\pm35°$ from the central meridian in order to minimize errors in the calculation of the electric-current parameters that arise due to the projection effect. The ARs were selected for the analysis according to the following criteria.

(1) The average magnetic flux of the region during AR monitoring time should be no less than 10^{21} Mx.

(2) The flare activity of the region during the observation period should be nonzero.

(3) When the AR location is within $\pm35°$ of the central meridian, it should be on the ascending branch of evolution or near the maximum of its evolution (the maximum evolution of the region was determined by the maximum spot area).

3. RESULTS AND DISCUSSION

Based on magnetographic data of the HMI/SDO instrument, we calculated the vertical and horizontal electric currents for an extended sample of 73 ARs during the time of their monitoring (see Table 1). The vertical currents were calculated using the integral method (Fursyak, 2018):

$$(I_z)_{i,j} = \frac{1}{\mu_0} \oint_L B_\perp dl,$$

where μ_0 is the magnetic constant, L is the closed contour (we used a 5×5 node (pixel) contour) around a pixel with coordinates $(i; j)$, and $B_\perp \equiv (B_x, B_y)$ are the transverse magnetic-field vector components in each pixel of the considered contour.

In order to estimate horizontal currents in photosphere, we applied the method described and analyzed in detail by Fursyak and Abramenko (2017). The formula to calculate the squared transverse electric current density is

$$j_\perp^2 \approx \frac{1}{\mu_0^2}\left[\left(\frac{\partial B_z}{\partial y}\right)^2 + \left(\frac{\partial B_z}{\partial x}\right)^2\right].$$

As before (Fursyak et al., 2020), a number of electric current and magnetic-field parameters were calculated with the developed IDL code for the analyzed regions.

— The total unsigned vertical electric current in the AR:

$$I_{z\,tot} = \Sigma |I_z|_{i,j}$$

— The average unsigned vertical electric current density in the AR:

Table 1. Main parameters of the magnetic fields and electric currents of the studied ARs (see description in the text)

NOAA	Time of AR monitoring	$\bar{\Phi}$	$\overline{I_{z\,\text{tot}}}$	$\langle|\overline{j_z}|\rangle$	$\langle|\overline{j_\perp}|\rangle$	$\overline{\rho_{jz}}$	$\overline{\rho_{Bz}}$	FI*	AR type
1	2	3	4	5	6	7	8	9	10
11 158	12.02.−15.02.2011	1.24	422.00	4.10	7.07	2.61	−2.08	83.28	B
11 261	31.07.−03.08.2011	1.27	489.19	4.21	10.10	2.33	−24.13	45.38	B
11 263	02.08.−05.08.2011	1.72	433.58	3.51	4.18	0.71	−8.57	8.32	B
11 283	04.09.−07.09.2011	0.99	317.59	3.13	3.98	5.36	−41.53	90.14	A
11 302	27.09.−30.09.2011	2.49	666.32	3.54	6.57	3.46	−37.26	10.72	A
11 305	29.09.−02.10.2011	0.62	187.72	3.29	6.27	5.80	−65.75	16.84	B
11 339	06.11.−10.11.2011	3.28	882.56	3.00	7.84	1.14	−30.66	12.08	A
11 391	07.01.−10.01.2012	0.98	287.93	2.76	9.34	4.59	−34.73	0.54	A
11 429	07.03.−10.03.2012	2.87	660.37	3.47	12.96	−4.33	8.87	167.78	B
11 476	09.05.−13.05.2012	3.00	892.31	3.98	9.34	0.16	−29.68	55.72	A
11 512	27.06.−30.06.2012	0.82	210.92	2.90	9.55	−1.63	22.24	1.90	A
11 520	10.07.−14.07.2012	5.80	1383.01	2.85	7.32	2.79	25.54	42.22	B
11 598	25.10.−29.10.2012	1.04	273.55	3.15	6.23	0.89	31.98	0.18	B
11 618	20.11.−23.11.2012	1.19	437.01	4.22	4.60	4.11	−21.23	22.16	A
11 654	12.01.−16.01.2013	2.82	723.33	3.06	7.57	0.39	−21.79	9.42	A
11 711	04.04.−07.04.2013	1.43	273.02	2.09	6.51	−0.76	59.27	0.68	A
11 748	18.05.−21.05.2013	0.49	191.43	3.40	7.28	2.22	−1.67	6.08	B
11 778	27.06.−30.06.2013	0.42	141.71	2.50	8.06	3.87	16.38	2.58	A
11 861	11.10.−14.10.2013	1.18	319.28	3.20	5.17	−2.46	−8.55	15.46	A
11 882	28.10.−01.11.2013	0.86	243.53	3.03	8.07	4.03	12.57	11.83	B
11 890	07.11.−10.11.2013	2.41	667.48	3.23	9.89	1.46	8.13	66.42	A
11 899	17.11.−20.11.2013	2.03	401.27	2.55	6.37	6.83	−82.11	0.34	U
11 936	27.12.−31.12.2013	0.95	304.99	3.18	3.85	5.39	22.25	43.37	A
11 944	06.01.−09.01.2014	5.38	1241.80	2.97	5.33	3.13	32.70	56.78	A
11 946	06.01.−09.01.2014	0.94	227.33	3.09	11.23	1.20	16.48	3.35	B
11 968	01.02.−05.02.2014	1.60	519.29	3.22	10.12	0.71	16.59	24.92	B
11 974	10.02.−13.02.2014	1.61	630.08	4.14	10.46	1.88	6.48	67.44	A
11 991	02.03.−05.03.2014	1.09	314.38	3.52	7.79	3.43	−2.92	10.50	B
12 002	12.03.−15.03.2014	1.14	295.69	3.01	7.71	0.60	1.52	0.90	A
12 014	24.03.−27.03.2014	0.96	268.45	2.67	8.16	3.62	50.71	1.08	B
12 017	25.03.−29.03.2014	0.68	185.24	3.02	8.20	2.64	−21.68	32.95	A
12 109	07.07.−10.07.2014	2.04	492.02	3.15	9.12	−0.23	50.35	2.22	B
12 149	26.08.−29.08.2014	0.68	181.78	2.75	3.69	6.92	−50.87	5.84	A
12 152	31.08.−03.09.2014	1.19	335.56	2.84	6.76	3.31	1.58	3.86	A
12 158	09.09.−12.09.2014	1.45	427.19	3.29	7.43	−1.39	44.28	33.48	B
12 192	22.10.−25.10.2014	9.53	2221.87	3.20	11.93	1.30	−17.06	234.00	B
12 205	08.11.−12.11.2014	1.23	427.23	3.53	8.58	4.03	−36.40	18.93	A
12 222	30.11.−04.12.2014	2.25	493.19	2.87	10.02	−0.20	29.06	29.73	A
12 241	17.12.−21.12.2014	2.03	530.79	3.38	10.38	0.89	3.92	22.13	A
12 253	03.01.−06.01.2015	2.02	510.41	2.91	11.50	0.63	15.52	17.28	A
12 268	27.01.−30.01.2015	1.65	419.28	2.84	6.52	4.24	24.54	22.32	A
12 277	01.02.−05.02.2015	1.72	468.75	2.60	7.17	4.62	11.96	6.20	B
12 290	22.02.−26.02.2015	0.42	88.65	2.04	5.49	3.44	0.60	0.17	A
12 297	11.03.−14.03.2015	1.58	563.54	4.62	4.40	3.59	47.14	116.02	B
12 303	21.03.−24.03.2015	0.40	97.15	2.20	5.74	3.49	−49.98	0.60	U
12 305	25.03.−29.03.2015	1.44	326.14	2.66	6.64	3.14	55.60	1.85	B
12 320	06.04.−09.04.2015	0.84	281.48	3.01	4.60	3.86	6.13	11.56	A

Table 1. (Contd.)

NOAA	Time of AR monitoring	$\bar{\Phi}$	$\overline{I_{z\,\text{tot}}}$	$\langle|\overline{j_z}|\rangle$	$\langle|\overline{j_\perp}|\rangle$	$\overline{\rho_{jz}}$	$\overline{\rho_{Bz}}$	FI*	AR type
1	2	3	4	5	6	7	8	9	10
12335	05.05.–08.05.2015	1.04	319.52	2.95	9.16	2.47	11.99	16.88	A
12339	10.05.–13.05.2015	2.95	782.15	2.83	6.86	2.55	−17.17	6.94	B
12365	09.06.–13.06.2015	0.36	107.96	2.88	4.81	−5.34	−51.96	2.83	B
12367	15.06.–19.06.2015	1.60	413.06	2.61	11.32	4.56	15.61	4.20	B
12371	20.06.–23.06.2015	2.97	679.66	3.23	8.60	−2.55	−11.28	33.68	B
12381	07.07.–10.07.2015	1.38	301.09	2.94	5.84	3.34	−11.57	2.42	A
12396	06.08.–09.08.2015	2.37	537.38	3.15	9.22	−1.50	10.97	7.60	B
12403	22.08.–25.08.2015	3.39	917.63	3.60	11.85	−0.98	5.45	51.46	A
12421	23.09.–27.09.2015	0.32	104.33	3.31	7.99	−1.62	28.47	0.28	B
12443	02.11.–05.11.2015	1.90	486.96	2.78	12.40	4.14	−35.35	9.72	A
12470	17.12.–21.12.2015	1.70	318.59	2.34	4.98	6.80	−39.63	3.57	U
12473	25.12.–30.12.2015	1.75	396.93	2.89	9.19	6.92	18.31	12.04	A
12480	10.01.–14.01.2016	0.58	104.82	2.26	6.84	1.06	−58.81	1.10	B
12492	05.02.–09.02.2016	0.28	85.43	2.69	7.06	5.56	−10.27	0.27	B
12494	05.02.–07.02.2016	0.73	174.81	3.00	9.68	−2.32	−22.13	2.95	B
12506	26.02.–01.03.2016	0.43	125.02	2.91	6.83	3.79	7.91	0.72	A
12521	13.03.–16.03.2016	0.35	96.81	2.86	10.90	1.53	−13.99	0.44	A
12529	12.04.–16.04.2016	2.87	561.99	2.74	8.76	3.54	−61.42	3.75	A
12546	18.05.–22.05.2016	1.77	340.71	2.60	5.77	5.21	78.38	0.17	U
12615	02.12.–05.12.2016	0.70	181.27	2.88	9.54	8.08	21.08	1.06	A
12644	27.03.–30.03.2017	0.81	187.35	2.88	3.09	3.64	−11.12	0.24	A
12661	05.06.–09.06.2017	0.26	84.05	2.41	6.69	6.90	25.19	0.67	A
12665	10.07.–13.07.2017	1.99	464.17	2.95	10.94	−0.38	27.48	5.90	A
12673	02.09.–05.09.2017	1.47	486.26	3.99	8.75	1.10	38.75	305.20	B
12674	03.09.–06.09.2017	2.47	475.29	2.49	4.76	−0.24	−20.54	0.42	A
12699	09.02.–12.02.2018	0.86	208.12	2.84	9.07	0.76	6.00	1.22	A

$\langle|j_z|\rangle = \dfrac{\sum|j_z|_{i,j}}{N}$, where N is the total number of pixels inside the bitmap and conf_disambig masks (the masks will be described below).

— The average unsigned horizontal electric current density:

$\langle|j_\perp|\rangle = \dfrac{\sum|j_\perp|_{i,j}}{N}$, where N is the total number of pixels inside the bitmap and conf_disambig masks, as in the previous case.

— The AR magnetic flux:

$\Phi = \sum|B|_{i,j} \times S$, where S is the pixel area in the HMI/SDO magnetogram (in cm^2).

— The electrical-current imbalance in the AR:

$\rho(j_z) = \dfrac{\sum\left|j_z^+(i,j)\right| - \sum\left|j_z^-(i,j)\right|}{\sum\left|j_z^+(i,j)\right| + \sum\left|j_z^-(i,j)\right|} \times 100\%$, where

$j_z^+(i,j)$ and $j_z^-(i,j)$ are the electric-current densities in pixel (i,j) in accordance with $j_z(i,j) > 0$ and $j_z(i,j) < 0$.

— The magnetic-flux imbalance:

$\rho(B_z) = \dfrac{\sum\left|B_z^+(i,j)\right| - \sum\left|B_z^-(i,j)\right|}{\sum\left|B_z^+(i,j)\right| + \sum\left|B_z^-(i,j)\right|} \times 100\%$, where

$B_z^+(i,j)$ and $B_z^-(i,j)$ are the magnetic-field strengths in pixel (i,j) in accordance with $B_z(i,j) > 0$ and $B_z(i,j) < 0$.

All electric-current parameters were calculated not inside the rectangular field corresponding to the SHARP magnetograms but inside two standard SHARP masks (Fig. 1): bitmap (outlines the AR boundaries) and conf_disambig (allows the selection of magnetogram pixels in which the 180° ambiguity of the determination of the transverse magnetic-field azimuth is corrected with a high degree of confidence). The magnetic-field parameters (magnetic flux and its imbalance) were calculated for the entire SHARP magnetogram, but, following Norton et al.
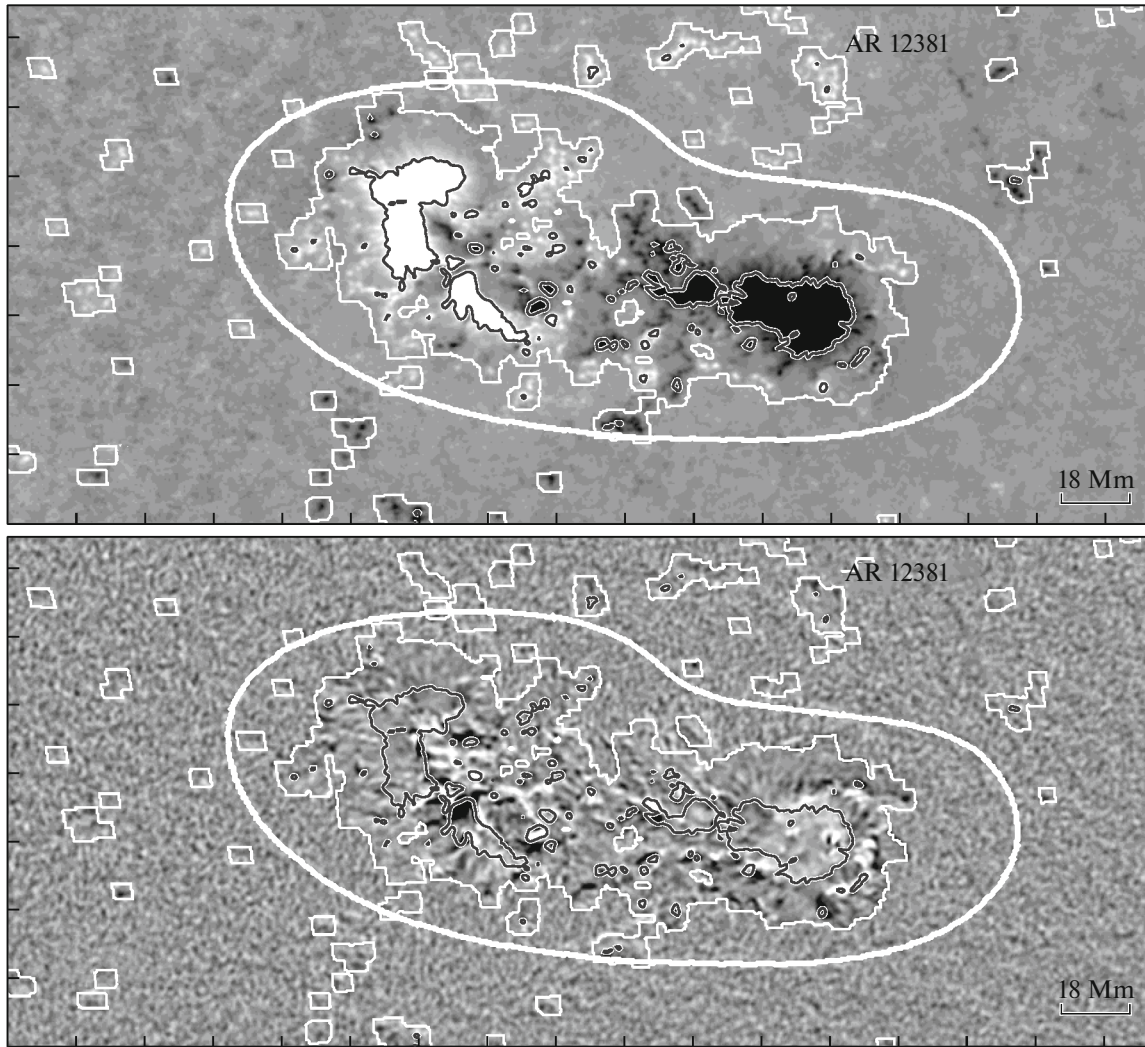
Fig. 1. Example of a magnetogram of the B_z component of the magnetic field vector in the photosphere (top) and the vertical electric current density map j_z (bottom) in the AR NOAA 12381 at the time of start of its monitoring (0000 UT July 07, 2015). The bold white contour indicates the bitmap mask, the thin white contour shows the conf_disambig mask (see the text), and the black contour indicates the regions in which the magnetic field exceeds the threshold of 600 G in absolute value.

(2017), we considered only pixels in which the absolute value of the magnetic field was at least 600 G. On the one hand, the choice of such a high threshold (the noise of the HMI/SDO instrument is about 17 G (Pesnell et al., 2012)) inevitably leads to lower magnetic flux values in the AR as compared to calculations performed with lower threshold values or without them. However, at the same time, we almost completely cut off the pixels in the peripheral part of the magnetogram (Fig. 1) occupied by local magnetic fields of several hundred gausses, which are mostly not directly related to the analyzed AR. This gives lower error values in the obtained results. The use of higher thresholds leads to the loss of significant information on the magnetic fields near the main spots of the considered AR.

We plotted the temporal-variation curves of all of the parameters analyzed during our observation period (3−6 days) (an example is shown in Fig. 2) and calculated the averaged values, which are summarized in Table 1.

The first column of Table 1 shows the AR number (NOAA), and the second column shows the time interval of the AR monitoring. The third to the eighth columns show the magnetic-flux values (in 10^{22} Mx units), the total unsigned vertical electric current $\overline{I_{z\,tot}}$ (in 10^{12} A units), the average densities of unsigned vertical $\langle\overline{|j_z|}\rangle$ and horizontal $\langle\overline{|j_\perp|}\rangle$ currents (in 10^{-3} A m^{-2} units), and the imbalances of the vertical current $\overline{\rho_{jz}}$ and magnetic flux $\overline{\rho_{Bz}}$ (in %) averaged over the moni-
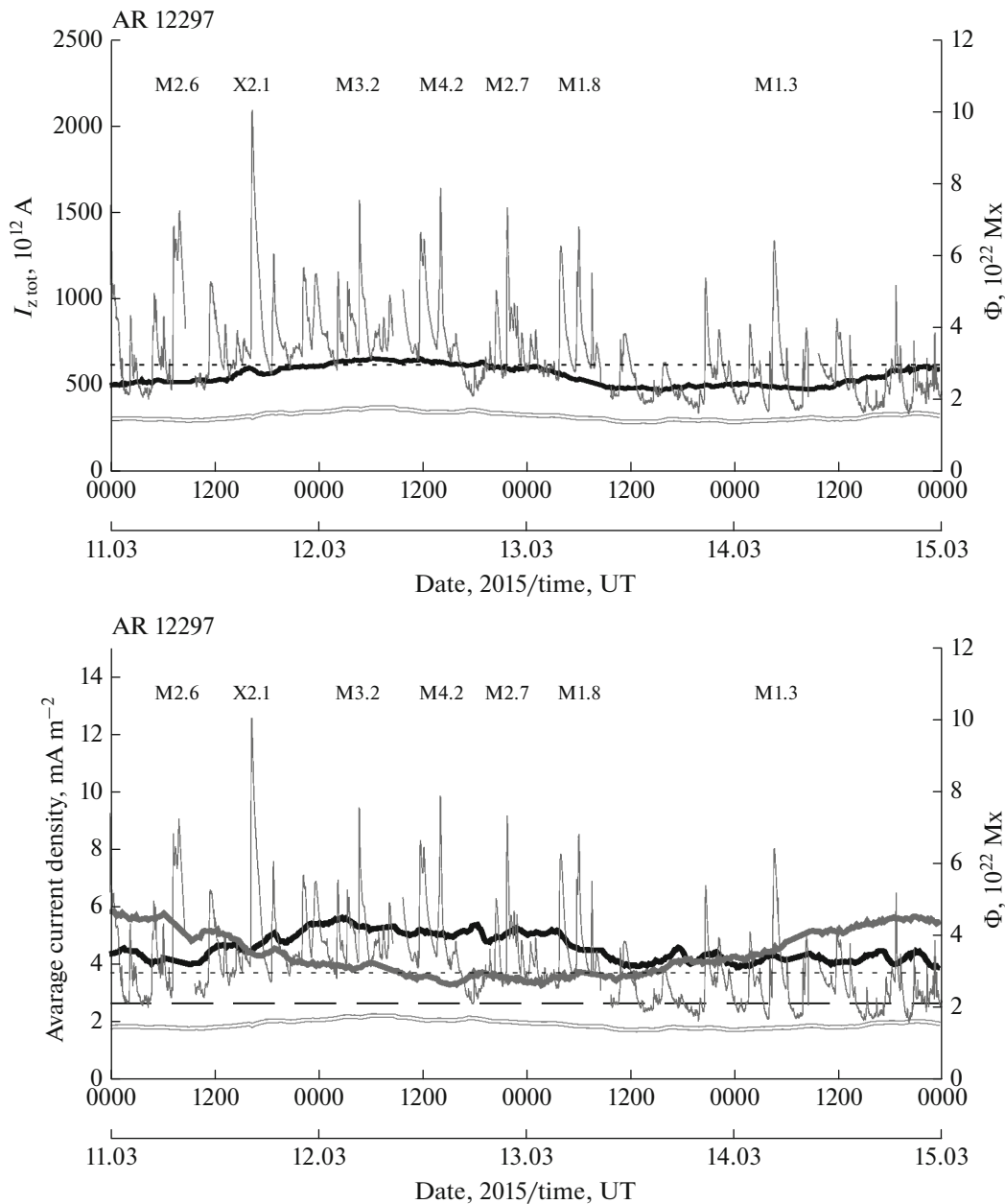
Fig. 2. Top: temporal variations of the total unsigned vertical electric current (solid black curve) and magnetic flux (double curve) for the AR NOAA 12297 during its monitoring. Variations of the total current, which are quasi-synchronous with the magnetic flux variations, can be clearly seen. Bottom: dynamics of the average unsigned vertical (solid black curve) and horizontal (solid gray curve) current densities for the same region. In both graphs, the thin, gray curve denotes the X-ray flux in the wavelength range of 1−8 Å in the Earth's orbit (according to data from the GOES-15 spacecraft). The X-ray classes of the most powerful flares associated with the studied AR are indicated.

toring time, respectively. The ninth (next-to-last) column of the table contains information on the flare index FI*, the parameter that characterizes the AR flare productivity. The classical notion of the flare index was introduced by V.I. Abramenko (2005) (formula (10) in this paper). The flare index is 1 (100) if one flare of X-ray class C1.0 (X1.0) is recorded in the AR daily during the period of its existence on the visible solar disk. However, here, taking into account the

experience of the previous study (Fursyak et al., 2020), we have slightly modified the formula for its calculation:

$$\text{FI*} = \frac{1.0 \sum{}^* C + 10 \sum{}^* M + 100 \sum{}^* X}{\tau^*} \times 100\%,$$

where $\sum{}^* C$, $\sum{}^* M$, and $\sum{}^* X$ are the sums of the scores of all flares of X-ray classes C, M, and X, respectively, recorded in the studied AR during time
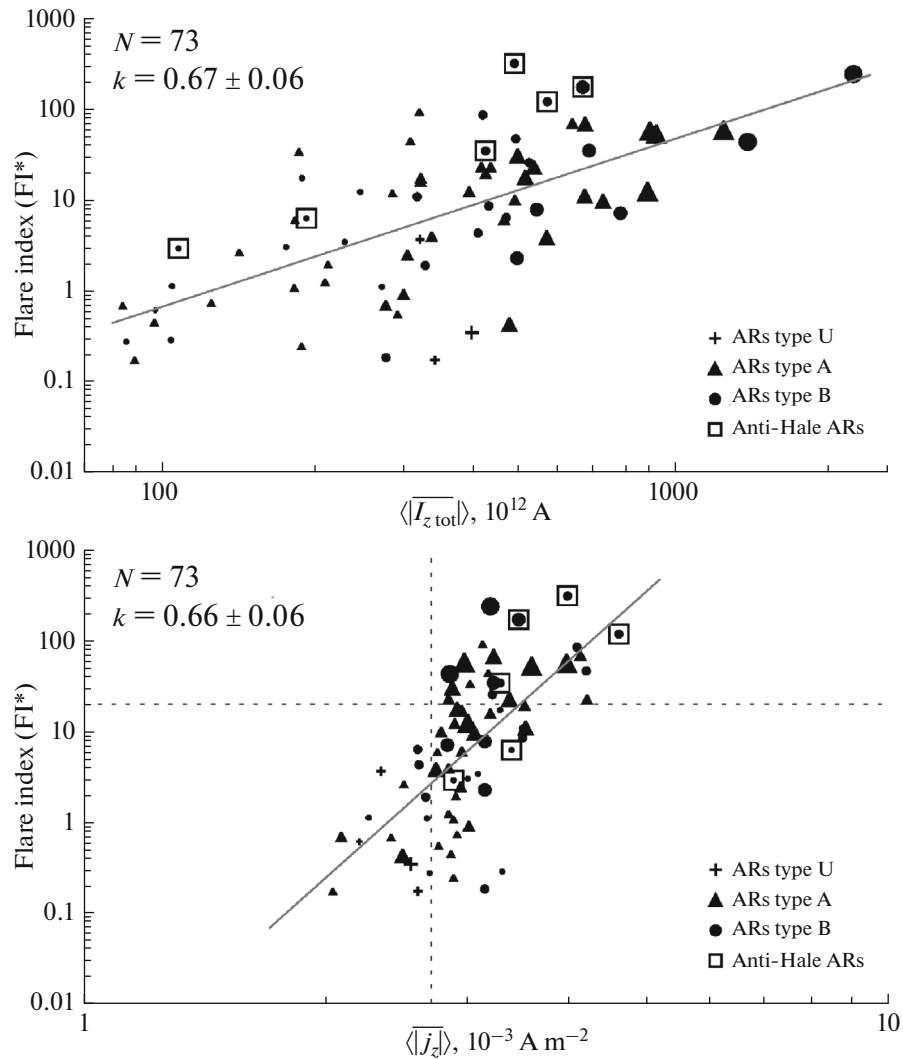
Fig. 3. Dependences of FI* on $\overline{I_{z\,tot}}$ (top) and FI* on $\langle\overline{|j_z|}\rangle$ (bottom) for the studied ARs. Crosses, U-type regions; triangles, A-type regions; circles, irregular B-type regions according to MMC. The size of the symbol in each case is proportional to the AR magnetic flux averaged over the monitoring period. The vertical dotted line in the lower diagram marks the "critical" level of the average unsigned vertical electric current density of 2.7×10^{-3} A m^{-2} (more detail is given in the text and by Fursyak et al. (2020)); the horizontal dotted line shows the reference level above which ARs with at least one recorded X-class X-ray flare during the monitoring period are located.

period $\tau^* = \tau' + 1$, the time of our monitoring of region (τ') with an added day. The addition of one day follows from our previous studies (Fursyak et al., 2020) that show that the time required for energy accumulation in the upper layers of the solar atmosphere and its realization in the powerful solar flares is about 20 hours when the electric-current parameters change abruptly.

Data from Table 1 is used below to determine the nature of the relationship between the electric-current parameters and the flare productivity of the AR (FI* value) in the first case and with the region type according to MMC in the second.

Figure 3 presents curves showing the correlation between the electric-current parameters and the AR flare productivity (i.e., the flare index FI*). Only the dependences with the highest correlation are shown: FI* vs $\overline{I_{z\,tot}}$ (correlation coefficient $k = 0.67$) and FI* vs $\langle\overline{|j_z|}\rangle$ (correlation coefficient $k = 0.66$). In Figure 3, different AR types according to MMC are marked by different symbols. The U-type regions are indicated by crosses, A-type regions are denoted by triangles, and B-type regions are shown by circles. Symbols placed in squares are ARs in which Hale's law is violated. The size of each symbol is proportional to the average magnetic flux of the region over the monitoring time.
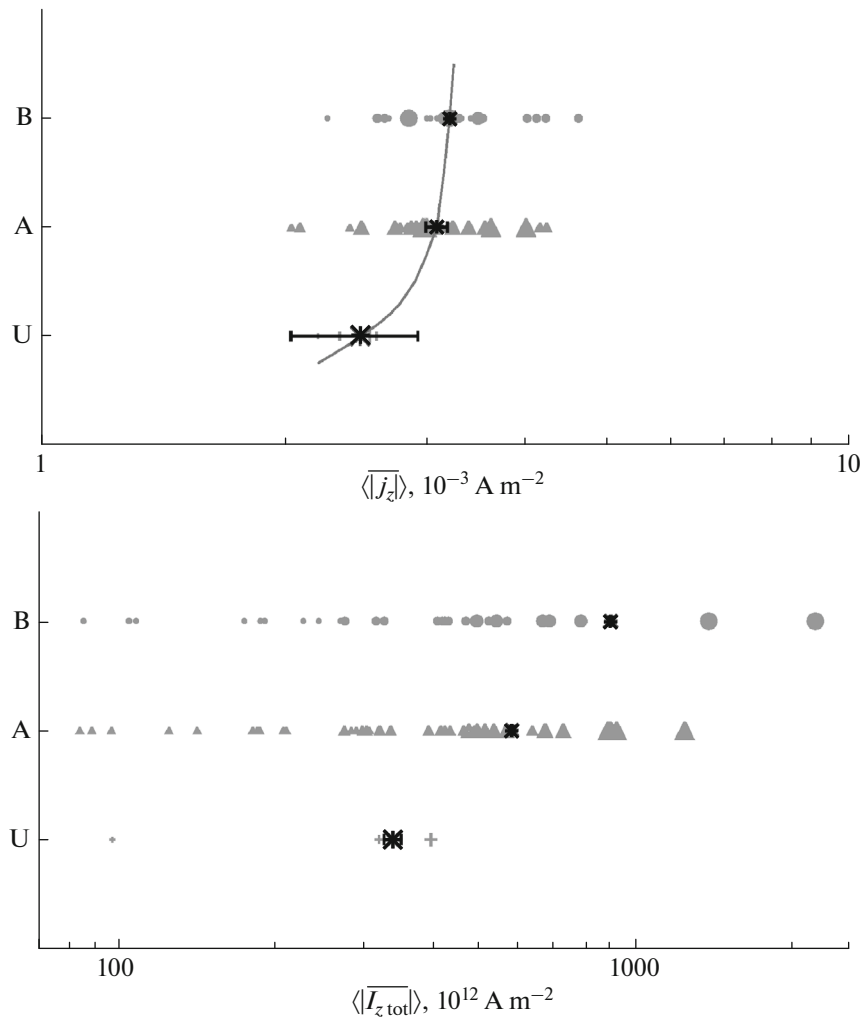
Fig. 4. Dependences of AR types on $\langle\overline{|j_z|}\rangle$ (top) and $\overline{I_{z\,\text{tot}}}$ (bottom) for the studied ARs. Asterisks mark the weighted average values of the corresponding electric-current parameters for the given AR type. Error bars are indicated.

In the top diagram of Fig. 3 (FI* vs $\overline{I_{z\,\text{tot}}}$), despite the significant spread of points, a general trend is observed: the flare productivity of the region increases with an increase in the total unsigned current.

The rather large spread of flare-activity values in the regions with the same values of the total unsigned current can be explained by the fact that only a small portion (a few percent) of the magnetic energy stored in the electric currents occurs in flares (Zaitsev et al., 1998).

Another feature noted in the top panel of Fig. 3 is that regions with low magnetic flux (indicated by small symbols) are grouped mainly in the left part of the diagram (up to $\overline{I_{z\,\text{tot}}} = (300-330) \times 10^{12}$ A), while the top right part of the diagram includes the regions with the highest magnetic flux (large symbols). Therefore, the value of the total unsigned current is proportional to the value of the magnetic flux of the AR. Actually, the same conclusion can be made if we compare columns 3 and 4 of Table 1 or the curves of temporal variations of the

total unsigned current and magnetic flux for any of the studied ARs (Fig. 2, top panel).

A different picture is observed if we consider the FI* dependence on $\langle\overline{|j_z|}\rangle$ (Fig. 3, bottom panel). First, we can see a relatively small spread of values of the average unsigned, vertical electric-current density for all studied ARs (within $\langle\overline{|j_z|}\rangle = (2-5) \times 10^{-3}$ A m^{-2}). It is also impossible to relate unambiguously the value of the average density of the vertical current to the magnetic flux of the region, as it was done for the total current: the symbols of different sizes are rather chaotically scattered across the diagram.

At the same time, the presence of the "critical" value $\langle\overline{|j_z|}\rangle \approx 2.7 \times 10^{-3}$ A m^{-2} (vertical dotted line in Fig. 3, bottom panel), which was determined in our earlier study (Fursyak et al., 2020), is confirmed: the solar flares of X-ray M and X classes are observed in the absolute majority of ARs with value $\langle\overline{|j_z|}\rangle$ above the

critical level (X-class flares are observed in the regions lying above the horizontal dotted line in the diagram), while only C-class flares are identified in most regions with $\left\langle \overline{|j_z|} \right\rangle < 2.7 \times 10^{-3}$ A m^{-2}.

However, it is extremely difficult to deduce the relationship between the electric-current parameters and the AR type according to MMC based on data presented in the graphs in Fig. 3, because different types of regions in the graphs are mixed up, and it is extremely difficult to identify any sequence (especially for regions of A and B types). Therefore, we remove the value of FI* from the graphs below and plot the dependence of the electric-current parameters on the AR type (Fig. 4).

Here, the differences in the values of the electric-current parameters in regions of different magneto-morphological classes are visible. The lowest values of the current parameters are typical of unipolar regions (type U according to MMC), and the highest values are observed in irregular regions (type B). It is extremely difficult to separate the regions of A and B types in $\left\langle \overline{|j_z|} \right\rangle$ − AR types (Fig. 4, top panel), because the difference in the weighted average values of $\left\langle \overline{|j_z|} \right\rangle$ calculated with the formula $\langle j \rangle = \dfrac{\sum \left(\left\langle \overline{|j_z|} \right\rangle \times \overline{\Phi} \right)_i}{\sum \Phi_i}$ is within the error limits (the gray asterisk marks the weighted average value in the graphs; the error bars are indicated). However, this difference is obvious for the pair of $\overline{I_{z\,\text{tot}}}$ − AR types (Fig. 4, bottom panel). Therefore, the proposal that the irregular B-type regions according to the MMC have higher reserves of "free" magnetic energy due to the additional work of the local dynamo, and, accordingly, higher values of the electric-current parameters is confirmed.

4. CONCLUSIONS

The study of current systems and their relation to the flare activity and features of the magnetic-field morphology, which was based on a sample of 73 ARs from solar cycle 24, led to the following conclusions:

(1) In all of the considered cases, the electric-current imbalance is quite low, no more than a few percent (the current imbalance of 61 ARs of the studied sample is under 5% in absolute value, and the maximum value is 8.08%). At the same time, the absolute values of the magnetic-current imbalance of the studied regions are significantly higher (only seven ARs show the field imbalance under 5%, and the maximum value of the imbalance reaches 82.11%).

(2) Of all of the analyzed electric current parameters, the highest correlation with the flare productivity of AR is observed for two values: the total unsigned vertical electric current $I_{z\,\text{tot}}$ (correlation coefficient $k = 0.67$) and the average unsigned vertical current density $\left\langle |j_z| \right\rangle$ (correlation coefficient $k = 0.66$).

(3) The difference in the values of the electric-current parameters of different AR types according to the MMC was found. The smallest values of the current parameters are typical of unipolar U-type regions, while the largest values are found in the B-type regions, which confirms the additional work of the local dynamo mechanisms in irregular regions, where the basic laws of the global dynamo are violated.

CONFLICT OF INTEREST

The authors declare that they have no conflicts of interest.

REFERENCES

Abramenko, V.I., Relationship between magnetic power spectrum and flare productivity in solar active regions, *Astrophys. J.*, 2005, vol. 629, no. 2, pp. 1141−1149.

Abramenko, V.I., Zhukova, A.V., and Kutsenko, A.S., Contributions from different-type active regions into the total solar unsigned magnetic flux, *Geomagn. Aeron. (Engl. Transl.)*, 2018, vol. 58, no. 8, pp. 1159−1169.

Aulanier, G., Démoulin, P., and Grappin, R., Equilibrium and observational properties of line-tied twisted flux tubes, *Astron. Astrophys.*, 2005, vol. 430, pp. 1067−1087.

Bobra, M.G., Sun, X., Hoeksema, J.T., et al., The Helioseismic and Magnetic Imager (HMI) vector magnetic field pipeline: SHARPS—Space-Weather HMI Active Region Patches, *Sol. Phys.*, 2014, vol. 289, no. 9, pp. 3549−3578.

Cheung, M.C.M. and Isobe, H., Flux emergence (theory), *Living Rev. Sol. Phys.*, 2014, vol. 11, no. 1, p. 3.

Dalmasse, K., Aulanier, G., Demoulin, P., et al., The origin of net electric currents in solar active regions, *Astrophys. J.*, 2015, vol. 810, no. 1, p. 17.

Fursyak, Yu.A., Vertical electric currents in active regions: Calculation methods and relation to the flare index, *Geomagn. Aeron. (Engl. Transl.)*, 2018, vol. 58, no. 8, pp. 1129−1135.

Fursyak, Yu.A. and Abramenko, V.I., Possibilities for estimating horizontal electrical currents in active regions on the Sun, *Astrophysics*, 2017, vol. 60, no. 4, pp. 544−552.

Fursyak, Yu.A., Abramenko, V.I., and Kutsenko, A.S., Dynamics of electric current's parameters in active regions on the Sun and their relation to the flare index, *Astrophysics*, 2020, vol. 63, no. 2, pp. 260−273.

Hale, G.E., Ellerman, F., Nicholson, S.B., and Joy, A.H., The magnetic polarity of sun-spots, *Astrophys. J.*, 1919, vol. 49, pp. 153−185.

Hoeksema, J.T., Liu, Y., Hayashi, K., et al., The Helioseismic and Magnetic Imager (HMI) vector magnetic field pipeline: Overview and performance, *Sol. Phys.*, 2014, vol. 289, no. 9, pp. 3483−3530.

Leka, K.D., Canfield, R.C., McClymont, A.N., and van Driel-Gesztelyi, L., Evidence for current-carrying emerging flux, *Astrophys. J.*, 1996, vol. 462, pp. 547−560.

Longcope, D.W. and Welsch, B.T., A model for the emergence of a twisted magnetic flux tube, *Astrophys. J.*, 2000, vol. 545, no. 2, pp. 1089−1100.

McClymont, A.N. and Fisher, G.H., On the mechanical energy available to drive solar flares, in *Solar System Plasma Physics: Geophysical Monograph Series 54*, Waite, J.H., Jr., Burch, J.L., and Moore, R.L., Eds., Washington, DC: American Geophysical Union, 1989, pp. 219−225.

McIntosh, P.S., The classification of sunspot groups, *Sol. Phys.*, 1990, vol. 125, no. 2, pp. 251−267.

Norton, A.A., Jones, E.H., Linton, M.G., and Leake, J.E., Magnetic flux emergence and decay rates for preceder and follower sunspots observed with HMI, *Astrophys. J.*, 2017, vol. 842, no. 1, p. 3.

Pesnell, W.D., Thompson, B.J., and Chamberlin, P.C., The Solar Dynamics Observatory (SDO), *Sol. Phys.*, 2012, vol. 275, pp. 3−15.

Scherrer, P.H., Schou, J., Bush, R.I., et al., The Helioseismic And Magnetic Imager (HMI) investigation for the Solar Dynamics Observatory (SDO), *Sol. Phys.*, 2012, vol. 275, nos. 1−2, pp. 207−227.

Schrijver, C.J., DeRosa, M.L., Metcalf, T., et al., Nonlinear force-free field modeling of a solar active region around the time of a major flare and coronal mass ejection, *Astrophys. J.*, 2008, vol. 675, no. 2, pp. 1637−1644.

Török, T. and Kliem, B., The evolution of twisting coronal magnetic flux tubes, *Astron. Astrophys.*, 2003, vol. 406, pp. 1043−1059.

Wang, J., Shi, Z., Wang, H., and Lue, Y., Flares and the magnetic nonpotentiality, *Astrophys. J.*, 1996, vol. 456, pp. 861−878.

Zaitsev, V.V., Stepanov, A.V., Urpo, S., and Pohjolainen, S., LRC-circuit analog of current-carrying magnetic loop: Diagnostics of electric parameters, *Astron. Astrophys.*, 1998, vol. 337, pp. 887−896.

Zhukova, A.V., Catalog of active regions of solar cycle 24, *Izv. Krym. Astrofiz. Obs.*, 2018, vol. 114, no. 2, pp. 74−86.

Translated by N. Semenova